Article

Measuring topological invariants for higher-order exceptional points in quantum three-mode systems

Check for updates

Pei-Rong Han [1,2], Wen Ning [1], Xin-Jie Huang[1], Ri-Hua Zheng[1], Shou-Bang Yang[1], Fan Wu[1], Zhen-Biao Yang [1,3] ✉, Qi-Ping Su[4], Chui-Ping Yang [4] ✉ & Shi-Biao Zheng [1,3] ✉

Owing to the presence of exceptional points (EPs), non-Hermitian (NH) systems can display intriguing topological phenomena without Hermitian analogs. However, experimental characterizations of exceptional topological invariants have been restricted to second-order EPs (EP2s) in classical or semiclassical systems. We here propose an NH multi-mode system with higher-order EPs, each of which is underlain by a multifold-degenerate multipartite entangled eigenstate. We implement the NH model by controllably coupling a Josephson-junction-based electronic mode to two microwave resonators. We experimentally quantify the topological invariant for an EP3, by mapping out the complex eigenspectra of the tripartite system along a loop surrounding this EP3 in the parameter space. The nonclassicality of the realized topology is manifested by the observed quantum correlations in the corresponding eigenstates. Our results extend research of exceptional topology to fully quantum-mechanical models with multipartite entangled eigenstates.

As one of the most well-tested physical theories, quantum mechanics has successfully passed numerous experimental tests. In most quantum-mechanical experiments, the system of interest is well isolated from its surrounding environment[1,2], so that its dynamics is governed by the Schrödinger equation with an energy operator often called Hamiltonian. The Hermiticity of the Hamiltonian ensures that the system evolves unitarily. However, any real quantum system is inevitably coupled to the environment[3], which functions by entangling its degrees of freedom with the system state[4]. Through this entanglement, the environment continuously monitors the system state, which inevitably produces a measurement backaction[5]. Under this disturbance, the system dynamics could significantly deviate from the unitary evolution even when it does not make any quantum jump. Mathematically, the state trajectory, associated with this conditional evolution, is also governed by a Schrödinger equation but with a non-Hermitian (NH) Hamiltonian[6].

Due to the non-Hermiticity, two or more eigenvectors of the NH Hamiltonian can coalesce into a single one with the same eigenenergy at exceptional points (EPs)[7,8]. These singularities can bring about many unique phenomena, exemplified by exotic topological phenomena that are absent in Hermitian systems[8–12]. The past two decades have witnessed a number of experimental explorations on the NH singular features, including spectral parity-time phase transitions[13–21], dynamical chiral behaviors[22–28], exceptional entanglement transitions[29], and NH topology[30–44]. The topological invariant of an NH system can be quantified in terms of the eigenvectors or the complex eigenenergies[8–12]. This is in distinct contrast with the Hermitian case, where the topology cannot be defined by the eigenenergies which are always real. So far, NH topology has been observed in several experiments, all of which were restricted to second-order EPs (EP2s) realized in classical systems[35–39] or with a classically-driven qubit[40–42]. Compared to EP2s, higher-order EPs can exhibit much richer topological

[1]Fujian Key Laboratory of Quantum Information and Quantum Optics, College of Physics and Information Engineering, Fuzhou University, Fuzhou, China. [2]School of Physics and Mechanical and Electrical Engineering, Longyan University, Longyan, China. [3]Hefei National Laboratory, Hefei, China. [4]School of Physics, Hangzhou Normal University, Hangzhou, China. ✉e-mail: zbyang@fzu.edu.cn; yangcp@hznu.edu.cn; t96034@fzu.edu.cn

properties[11,12,43–45], and the associated spectral topological invariants are defined in a fundamentally different manner[12]. Despite the fundamental interest, such invariants have not been unambiguously characterized in experiment.

We here investigate both theoretically and experimentally the quantum-mechanical exceptional topology associated with higher-order EPs in an NH composite system consisting of multiple interacting modes. These EPs result from continuous and nonunitary evolutions in the single-excitation subspace without quantum jumps[46]. The topological property associated to each higher-order EP can be quantified by the homotopy invariant, recently proposed by Delplace et al.[12]. We experimentally engineer the NH three-mode system in a superconducting circuit, where a nonlinear Xmon mode is controllably coupled to two photonic modes stored in two separated microwave resonators. The non-Hermiticity of the system is manifested by the non-negligible dissipation of one photonic mode. We find that the resulting NH Hamiltonian possesses four EP3s in the real parameter space. We quantify the homotopy invariant associated to the EP3 in the first quadrant of the parameter space, by mapping out the eigenenergies of the NH Hamiltonian along a loop surrounding this EP3. The system eigenenergies are extracted from the output states of the three-mode system in the single-excitation subspace, measured for different evolution times. As far as we know, this is the first experimental characterization of the topological invariant associated with a higher-order EP. We further note that the winding number defined by Eq. (3) is zero for the degenerate points in both the two-dimensional (2D) and 3D Hermitian systems, referred to as diabolical points (DPs), as well as for EP2s in a 2D NH system, as detailed in the Supplementary Material. Therefore, such a winding number serves as a homotopy invariant that uniquely characterizes the topology of EP3s.

Results

NH multi-mode system

The system under consideration corresponds to a multi-mode system with competing coherent nearest-neighboring interactions and incoherent dissipation, as shown in Fig. 1a. Under the competition, the system evolution is a weighted mixture of infinitely many trajectories, among which of special interest is the one without quantum jump. This trajectory is governed by the NH Hamiltonian (setting $\hbar = 1$)

$$H_{\mathrm{NH}} = -\frac{1}{2}i\sum_{j=1}^{N}\kappa_j a_j^\dagger a_j + \sum_{j=1}^{N-1}\lambda_j(a_j^\dagger a_{j+1} + \mathrm{H.c.}), \quad (1)$$

where $a_j^\dagger$ and a_j denote the creation and annihilation operators of the jth mode with a decaying rate κ_j, λ_j represents the coupling coefficient between the jth and $(j+1)$th modes, and H.c. is the Hermitian conjugate. The excitation number of the total system is conserved along the no-jump trajectory, as the excitation number operator, $N_e = \sum_{j=1}^{N} a_j^\dagger a_j$, commutes with H_{NH}. Hereafter, we will consider the system behaviors restricted in the single-excitation subspace $\{|1_0 2 \ldots 0_N\rangle, \ldots, |0_1 \ldots 0_{N-1} 1_N\rangle\}$, where $|0_j\rangle$ and $|1_j\rangle$ respectively denote the ground and first excited states for the jth mode with j ranging from 1 to N.

For $\kappa_j = 0$ ($j = 1, \ldots, N$), the Hamiltonian (1) has N real eigenenergies, which display an N-fold degeneracy for $\lambda_j = 0$. When one or more modes are subjected to dissipations, the eigenenergies become complex. The resulting spectral structure can display exotic topological features without Hermitian analogs. To clearly illustrate the underlying NH quantum topological physics, we consider a three-mode system. For simplicity, we assume $\kappa_2 = \kappa_3 = 0$ and drop off the subscript of κ_1. Figure 1b, c shows the maximal real (imaginary) part of the gaps among the three complex eigenenergies versus λ_1 and λ_2. The results clearly
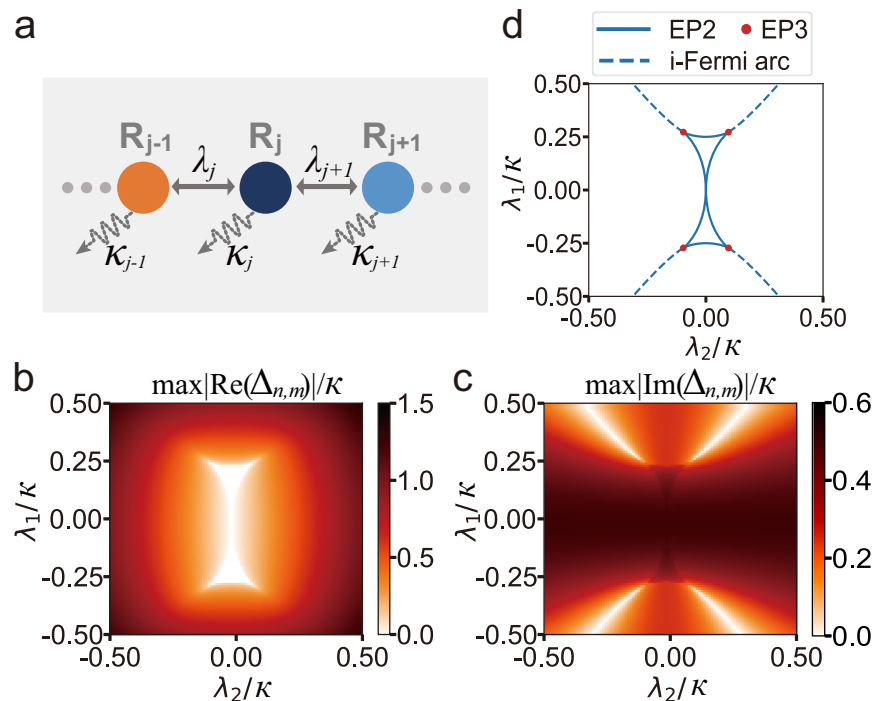

Fig. 1 | Sketch of the NH multi-mode system and the spectral structure.
a Theoretical model. The system involves N modes (R_j), arranged in a linear array. The NH Hamiltonian dynamics features the competition between the nearest-neighbor swapping couplings (λ_j) and the energy dissipations (κ_j). **b, c** Maxima for the real (**b**) and imaginary (**c**) gaps versus λ_1 and λ_2 in the three-mode system. For simplicity, we set $\kappa_2 = \kappa_3 = 0$, and assume κ_1 has a fixed nonzero value κ. At the three-

fold degeneracy points $\{\pm\lambda_1^c, \pm\lambda_2^c\}$, the maximum gap among the three complex eigenenergies vanishes. Here the parameters λ_1 and λ_2 are scaled in units of κ. $\Delta_{n,m}$ denotes the difference between two eigenenergies, i.e., $E_n - E_m$ ($n \neq m$, $n, m = 1, 2, 3$). **d** The solid lines denote EP2s where a pair of eigenstates coalesce. Along the dashed lines, all three eigenenergies have the same imaginary part. Their intersection points (red dots) are EP3s connecting Fermi arcs and i-Fermi arcs.
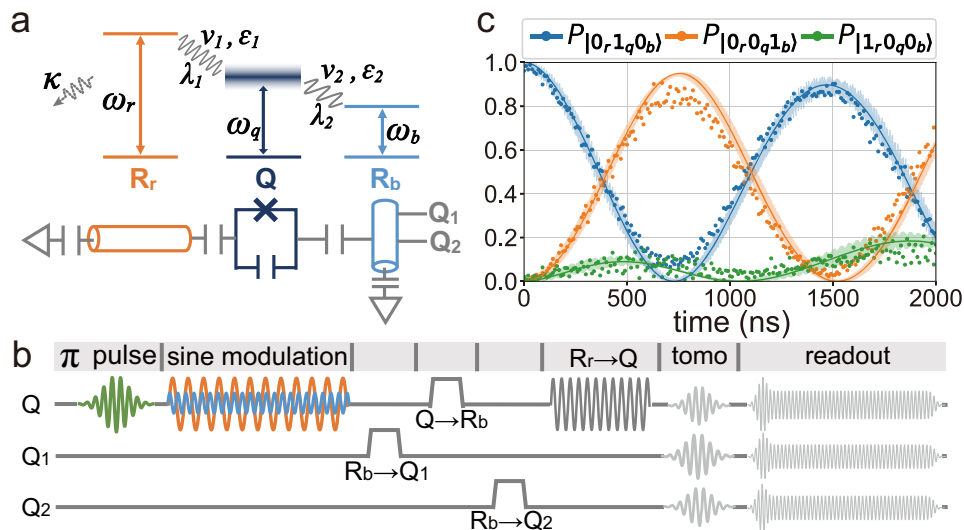
Fig. 2 | Experimental implementation. a Synthesis of the NH three-mode system. The NH Hamiltonian is realized in a circuit, where a Josephson-junction-based qubit (Q), together with a bus resonator (R_b) and a readout resonator (R_r), comprises an effective three-mode system in the single-excitation subspace. The decaying rates of Q and R_b are respectively 0.06 MHz and 0.08 MHz, both of which can be neglected compared to that of R_r, $\kappa = 5$ MHz. Q is coupled to R_r (R_b) at the first upper (lower) sideband with respect to the first (second) parametric modulation. **b** Pulse sequence. The qubit Q is first prepared in the excited state at its idle frequency, followed by the application of two sine modulations. The modulation frequencies (ν_1, ν_2) and amplitudes are tunable for controlling λ_1 and λ_2. After the modulating pulse, the evolved R_r-Q-R_b output state is mapped to the Q-Q_2-Q_1 system for readout, where Q_1 and Q_2 are two ancilla qubits, each of which can be controllably coupled to the bus resonator. **c** Observed evolutions of the populations. All data are measured for the initial state $|0_r1_q0_b\rangle$ at the point $\lambda_1 = 2\pi \times 0.21$ MHz and $\lambda_2 = 2\pi \times 0.31$ MHz. The results are obtained by discarding the measurement outcome $|0_r0_q0_b\rangle$ and renormalizing the remaining populations of $|0_r0_q1_b\rangle$, $|0_r1_q0_b\rangle$, and $|1_r0_q0_b\rangle$ in the single-excitation subspace. The solid curves are theoretical predictions using the NH Hamiltonian (1), while the fast oscillating curves are numerical simulation results using the original Hamiltonian (given in Section S3 of the Supplementary material) with frequency modulations included.

show that the non-Hermiticity splits the real degeneracy into four EP3s at $\{\pm\lambda_1^c, \pm\lambda_2^c\}$ with $\lambda_1^c = \sqrt{2}\kappa/3\sqrt{3}$ and $\lambda_2^c = \kappa/6\sqrt{3}$. At each EP3, the three eigenenergies have a vanishing real part and the same nonzero imaginary part.

The spectrum of the NH Hamiltonian exhibits a rich structure, where each of the four EP3s is connected to two curves of EP2s (solid lines in Fig. 1d), at which a pair of eigenstates and eigenenergies coalesce. The details of these eigenenergies are shown in Section S5 of the Supplementary Material. Enclosed in the EP2 contour is an iso-frequency region, where all three eigenenergies have the same real part. This is a 2D generalization of the linear-like two-fold degenerate Fermi arc, which connects 2 EP2s existing in a 2D system[30]. In the isofrequency region, the real parts of the three complex eigenenergies vanish, so that the state evolution of the system is determined by the imaginary parts of these eigenenergies, each of which corresponds to a gaining or losing rate depending upon its sign. After a long-time evolution, only the eigenvector with the largest imaginary part can survive for the no-jump case. Since such an eigenvector is essentially a tri-partite entangled state, the dynamics in the isofrequency region provides a way for robust generation and conditional stabilization of tripartite entanglement[47]. Such an entanglement generation and stabilization process is illustrated by the simulations presented in Section S2 of the Supplementary Material.

In addition to the real Fermi arc, each of the four EP3s emanates an i-Fermi arc (dashed lines in Fig. 1d)[11], along which the imaginary parts are three-fold degenerate. With a global shift of the spectrum by a suitable imaginary value, the four i-Fermi arcs correspond to the regions where the eigenenergies are all real. In view of spectral phase transitions, each of the four EP3s corresponds to a tripoint, where three distinct phases (featuring imaginary, real, and complex energy gaps) meet together.

Experimental implementation

We perform the experiment using a circuit quantum electrodynamics device with five nonlinear Xmon modes (qubits), each controllably coupled to the common bus resonator (R_b) of a fixed frequency $\omega_b/2\pi = 5.58$ GHz. The NH quantum multipartite system is realized with one of these qubits (labeled as Q), the bus resonator R_b, and the readout resonator of Q, (R_r), which has a frequency $\omega_r/2\pi = 6.66$ GHz. The on-resonance coupling strength between Q and R_b (R_r) is $g_b = 2\pi \times 20$ MHz ($g_r = 2\pi \times 41$ MHz). The decaying rate of Q (R_b) is 0.06 (0.08) MHz, which is two orders smaller than that of R_r ($\kappa = 5$ MHz). Thus, the dissipations of Q and R_b are negligible. To realize the NH tripartite Hamiltonian in a controllable manner, two parametric modulations are simultaneously applied to Q to modulate its transition frequency as $\omega_q = \omega_0 + \sum_{j=1,2} \varepsilon_j \cos(\nu_j t)$, where ω_0 is the mean frequency of Q, and ε_j and ν_j respectively denote the amplitude and frequency of the jth modulation, as depicted in Fig. 2a. Under the condition $\omega_0 + \nu_1 = \omega_r$, the qubit Q interacts with the readout resonator R_r at the first upper sideband for the first modulation, with the strength $\lambda_1 = g_r J_1(\varepsilon_1/\nu_1)$. Here, $J_1(\mu)$ is the first-order Bessel function of the first kind. The second modulation is used to induce the sideband interaction between Q and R_b, with the effective photonic swapping rate λ_2 controlled by ε_2. The sideband interactions and the system parameters are detailed in Section S3 of the Supplementary Material. When the R_r-Q-R_b system initially has one excitation, its dynamics, associated with no-jump trajectory, is described by the NH Hamiltonian (1) with $N = 3$, where R_r, Q, and R_b correspond to three modes sharing a single excitation.

The experiment starts with the preparation of an initial single-excitation state, following which the parametric modulations are applied to Q, with the experimental pulse sequence depicted in Fig. 2b. After a preset interaction time t, the parametric modulations are switched off to have Q decoupled from both R_b and R_r. The output state of the system, associated with the no-jump trajectory, is given by

$$|\psi(t)\rangle = c_1(t)|0_r0_q1_b\rangle + c_2(t)|0_r1_q0_b\rangle + c_3(t)|1_r0_q0_b\rangle. \quad (2)$$

Here the subscripts r, q, and b label R_r, Q, and R_b, respectively. As the excitation is conserved by the NH Hamiltonian while the quantum
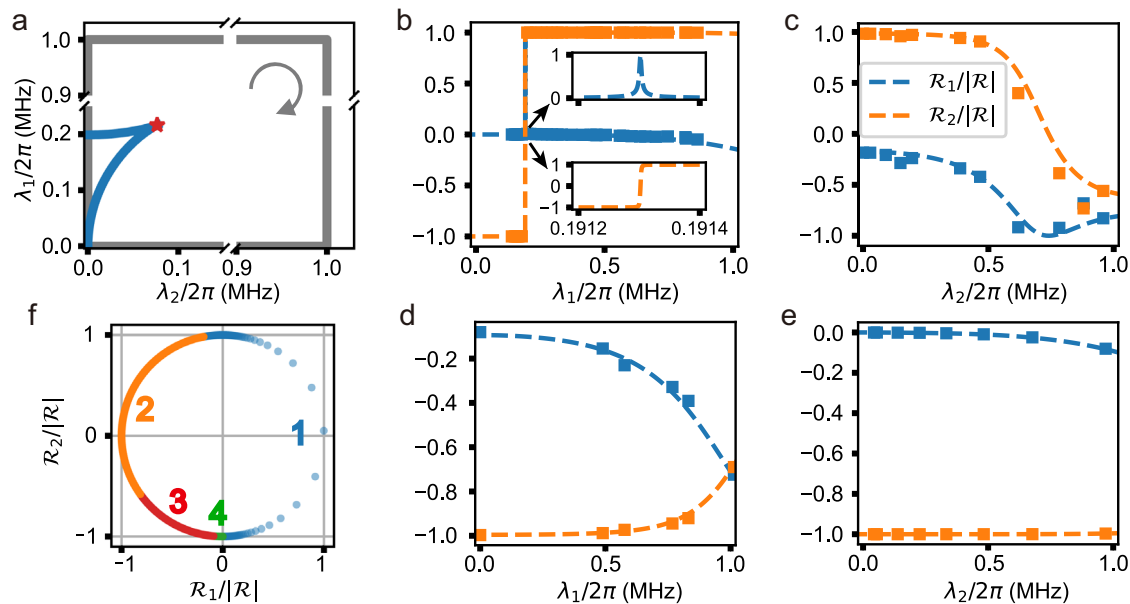
Fig. 3 | Characterization of the NH topology. a Loop traversed for extracting the winding number. The loop (gray solid line) is square-shaped with four vertices $(0, 0)$, $(\lambda_m, 0)$, $(0, \lambda_m)$, and (λ_m, λ_m), where $\lambda_m = 2\pi \times 1$ MHz. This loop surrounds an EP3 (red star), which connects two Fermi arcs consisting of EP2s (blue solid line). The arrow denotes the direction of the integral along the loop. **b**, **e** Normalized resultant vectors measured against λ_1 with $\lambda_2 = 0$ (**b**) and λ_m (**d**), and against λ_2 with $\lambda_1 = \lambda_m$ (**c**) and 0 (**e**). The squares represent the components $\mathcal{R}_1/|\mathcal{R}|$ (blue) and $\mathcal{R}_2/|\mathcal{R}|$ (orange), respectively. The dotted lines denote the fitted $\mathcal{R}_1/|\mathcal{R}|$ and $\mathcal{R}_2/|\mathcal{R}|$ as functions of λ_1 or λ_2. The winding number, calculated with these fitted functions, is 1. **f** Trajectory of the rescaled unit resultant vector $\mathcal{R}^u = (\mathcal{R}_1 + i\mathcal{R}_2)/|\mathcal{R}|$. The symbols "1", "2", "3", and "4", label the sections associated with the four edges of the parameter-space loop, shown in (**b**–**e**), respectively.

jump breaks down this conservation, the no-jump state trajectory can be postselected by discarding the outcome with null excitation. The joint tripartite output state is read out with the assistance of two ancilla qubits, denoted as Q_1 and Q_2. The R_r-Q-R_b output state is mapped to the Q-Q_2-Q_1 system, which is realized by swapping gates (see Section S4 in the Supplementary Material). Bloch vectors of the three qubits along different axes are then measured. By correlating the outcomes of these measurements, the three-qubit density matrix is reconstructed. Removing the ground state element and renormalizing the remaining ones, we obtain the final state of the system evolving under the NH Hamiltonian. With a correction for the infidelity of the state mapping, the resulting Q-Q_2-Q_1 output state corresponds to the R_r-Q-R_b output state right before the state mapping. Figure 2c shows the evolution of the populations $|0_r, 0_q1_b\rangle$, $|t0_r1_q0_bt\rangle$, and $|1_r0_q0_b\rangle$ for the initial state $|0_r1_q0_b\rangle$, measured at the point $\lambda_1 = 2\pi \times 0.21$ MHz and $\lambda_2 = 2\pi \times 0.31$ MHz. These populations are obtained by discarding the measurement outcome $|0_r0_q0_b\rangle$ and then renormalizing the probabilities for occurrences of the three single-excitation outcomes.

Measurement of the winding number

The topological invariant associated with each EP3 can be quantified by the winding number, calculated in terms of the resultant vector $\mathcal{R}$[12]

$$\mathcal{W} = \frac{1}{2\pi} \sum_{j=1,2} \oint_{C_\lambda} \frac{1}{\|\mathcal{R}\|^2} \left(\mathcal{R}_1 \frac{\partial \mathcal{R}_2}{\partial \lambda_j} - \mathcal{R}_2 \frac{\partial \mathcal{R}_1}{\partial \lambda_j} \right) d\lambda_j, \quad (3)$$

where the integral loop C_λ encloses the EP3 in the 2D parameter space. $\mathcal{R}_1$ and $\mathcal{R}_2$ depend upon the eigenenergies (for details, see Section S7 in the Supplementary Material), which can in principle be extracted from the output states measured for different interaction times. To simplify the measurement, we choose a square-shaped loop on the λ_1–λ_2 plane. The loop has four vertices $(0, 0)$, $(\lambda_m, 0)$, $(0, \lambda_m)$, and (λ_m, λ_m), as shown in Fig. 3a. With this choice, the eigenspectrum can be extracted in a relatively easy manner (see Section S5 in the Supplementary Material). In our experiment, λ_m is set to be $2\pi \times 1$ MHz.

The eigenenergies, measured along the four edges of the square-shaped loop, are detailed in Section S8 of the Supplementary Material. For different values of λ_1 or λ_2, $\mathcal{R}_1$, and $\mathcal{R}_2$ are calculated from the corresponding measured eigenenergies, as shown in Fig. 3b–e. The dashed lines denote the functions fitted with the measured data. We note that the rescaled unit resultant vector, defined as $\mathcal{R}^u = (\mathcal{R}_1 + i\mathcal{R}_2)/|\mathcal{R}|$, is changed along a circle when the control parameter (λ_1, λ_2) is varied along a loop enclosing the EP3, as illustrated in Fig. 3f. On the edge with $\lambda_2 = 0$, there is an EP2, within the vicinity of which the resultant vector undergoes a π rotation, as detailed in the insets of Fig. 3b. This rotation occurs in a very narrow region of the control parameter (λ_1, λ_2), but contributes half of the circular trajectory of $\mathcal{R}^u$. The winding number based on thus-obtained $\mathcal{R}_1$ and $\mathcal{R}_2$ is $\mathcal{W} = 1$, which confirms that the loop encircles an EP3. In addition to the EP3, the loop surrounds infinitely multiple EP2s, which form two exceptional arcs that cross at the EP3, as illustrated in Fig. 3a. These EP2s have no contribution to the characterized topological invariant, which corresponds to the winding number of the relative angle between $\mathcal{R}_1$ and $\mathcal{R}_2$[12]. This implies that the spectral topological features of higher EPs are fundamentally distinct from those of EP2s. As detailed in ref. 12, the winding number defined in Eq. (3) is the simplest example of the homotopy invariants, which can quantify topological properties of multifold symmetry-protected EPs but have not been experimentally characterized so far.

In a recent acoustic experiment[43], the measured local phase rigidities of the eigenvectors near an EP3 have a critical exponent coinciding with the winding number quantifying the calculated global Berry phase. However, the Berry phase itself, which characterizes the topological charge associated to the eigenvectors, has not been experimentally extracted, and neither has the eigenspectral topological invariant. In a recent experiment[48], a third-order exceptional line was observed with a nitrogen-vacancy system, where the NH Hamiltonian for a single electron with three levels was constructed by the dilation method. However, the topological properties of the realized EP3 have not been experimentally characterized. As far as we know,

our work represents the first measurement of homotopy invariants, of which the winding number for EP3s is the simplest example[12].

To reveal the quantum correlations among the three modes, we perform quantum state tomography on the output state of the system. For different values of the control parameters, the evolutions of the measured pairwise concurrences are detailed in Section S5 of the Supplementary Material. For the edges $\lambda_1 = 0$ and $\lambda_2 = 0$, the system reduces to a two-mode system, so that the eigenstates can be extracted from the state evolution in a relatively easy way. At point $(0, \lambda_m)$, the measured concurrences of the two eigenstates ($|\Phi_\pm\rangle$) for the R_b-Q subsystem, which is decoupled from R_r, are 0.997 and 0.997, respectively. At point $(\lambda_m, 0)$, the concurrences for two measured Q-R_r eigenstates ($|\Phi'_\pm\rangle$) are respectively 0.971 and 0.971. When $\lambda_1 \neq 0$ and $\lambda_2 \neq 0$, each of the three eigenstates corresponds to a tripartite entangled eigenstate, for which each mode is quantum-mechanically correlated to either of the other two modes. Experimental extraction of these eigenstates is a challenging task because each eigenstate involves four parameters to be determined. However, the observation of tripartite entangled states evolved from the initial product state $|0_b 1_q 0_r t\rangle$, indicate*s* that there exists tripartite entanglement in the underlying eigenstates. These observed nonclassical correlations represent another unique feature that fundamentally distinguishes the presently observed topology from those previously demonstrated in classical or semiclassical systems[30–45].

Discussion

In conclusion, we have investigated the exceptional topology in interacting many-body quantum systems, with a competition between coherent couplings and incoherent dissipation. The quantum topology is manifested by the presence of multiple higher-order EPs, each of which carries a quantized topological charge and is associated with a multifold degenerate eigenstate displaying highly nonclassical correlations. The NH model is experimentally realized with a superconducting qubit, which is correlated to a lossless bus resonator and a decaying readout resonator by swapping a single photon. The topological charge at each EP3 is quantified by the winding number, extracted from the eigenspectra measured with the assistance of two ancilla qubits. Each of the corresponding eigenstates exhibits quantum entanglement, confirming the nonclassical origin of the topology. Besides fundamental interest, the demonstrated NH dynamics associated with higher-order EPs may have applications in quantum technologies, such as sensitivity enhancement in quantum metrology[49] as well as fast and robust generation of quantum entanglement[50].

Data availability

The data that support the findings of this study are available from the corresponding author upon request.

References

1. Wineland, D. J. Nobel Lecture: superposition, entanglement, and raising Schröinger's cat. *Rev. Mod. Phys.* **85**, 1103–1114 (2013).
2. Haroche, S. Nobel Lecture: controlling photons in a box and exploring the quantum to classical boundary. *Rev. Mod. Phys.* **85**, 1083–1102 (2013).
3. Scully, M. O. & Zubairy, M. S. *Quantum Optics* (Cambridge, 2000).
4. Zurek, W. H. Decoherence, einselection, and the quantum origins of the classical. *Rev. Mod. Phys.* **75**, 715–775 (2003).
5. Ashida, Y., Gong, Z. & Ueda, M. Non-Hermitian physics. *Adv. Phys.* **69**, 249–435 (2020).
6. Bender, C. M. & Boettcher, S. Real spectra in non-Hermitian Hamiltonians having $\mathcal{PT}$ symmetry. *Phys. Rev. Lett.* **80**, 5243–5246 (1998).
7. Özdemir, Ş. K., Rotter, S., Nori, F. & Yang, L. Parity-time symmetry and exceptional points in photonics. *Nat. Mater.* **18**, 783–798 (2019).
8. Ding, K., Fang, C. & Ma, G. Non-Hermitian topology and exceptional-point geometries. *Nat. Rev. Phys.* **4**, 745–760 (2022).
9. Bergholtz, E. J., Budich, J. C. & Kunst, F. K. Exceptional topology of non-Hermitian systems. *Rev. Mod. Phys.* **93**, 015005 (2021).
10. Gong, Z. et al. Topological phases of non-Hermitian systems. *Phys. Rev. X* **8**, 031079 (2018).
11. Mandal, I. & Bergholtz, E. J. Symmetry and higher-order exceptional points. *Phys. Rev. Lett.* **127**, 186601 (2021).
12. Delplace, P., Yoshida, T. & Hatsugai, Y. Symmetry-protected multifold exceptional points and their topological characterization. *Phys. Rev. Lett.* **127**, 186602 (2021).
13. Choi, Y. et al. Quasieigenstate coalescence in an atom-cavity quantum composite. *Phys. Rev. Lett.* **104**, 153601 (2010).
14. Xiao, L. et al. Observation of critical phenomena in parity-time-symmetric quantum dynamics. *Phys. Rev. Lett.* **123**, 230401 (2019).
15. Öztürk, F. E. et al. Observation of a non-Hermitian phase transition in an optical quantum gas. *Science* **372**, 88–91 (2021).
16. Peng, P. et al. Anti-parity-time symmetry with flying atoms. *Nat. Phys.* **12**, 1139–1145 (2016).
17. Li, J. et al. Observation of parity-time symmetry breaking transitions in a dissipative Floquet system of ultracold atoms. *Nat. Commun.* **10**, 855 (2019).
18. Wu, Y. et al. Observation of parity-time symmetry breaking in a single-spin system. *Science* **364**, 878–880 (2019).
19. Naghiloo, M., Abbasi, M., Joglekar, Y. N. & Murch, K. W. Quantum state tomography across the exceptional point in a single dissipative qubit. *Nat. Phys.* **15**, 1232–1236 (2019).
20. Wang, Z. et al. Observation of the exceptional point in superconducting qubit with dissipation controlled by parametric modulation. *Chin. Phys. B* **30**, 100309 (2021).
21. Gao, T. et al. Observation of non-Hermitian degeneracies in a chaotic exciton-polariton billiard. *Natrue* **526**, 554–558 (2015).
22. Zhang, X.-L., Wang, S., Hou, B. & Chan, C. T. Dynamically encircling exceptional points: in situ control of encircling loops and the role of the starting point. *Phys. Rev. X* **8**, 021066 (2018).
23. Doppler, J. et al. Dynamically encircling an exceptional point for asymmetric mode switching. *Nature* **537**, 76–79 (2016).
24. Xu, H., Mason, D., Jiang, L. & Harris, J. G. E. Topological energy transfer in an optomechanical system with exceptional points. *Nature* **537**, 80–83 (2016).
25. Yoon, J. W. et al. Time-asymmetric loop around an exceptional point over the full optical communication band. *Nature* **562**, 86–90 (2018).
26. Liu, W., Wu, Y., Duan, C.-K., Rong, X. & Du, J. Dynamically encircling an exceptional point in a real quantum system. *Phys. Rev. Lett.* **126**, 170506 (2021).
27. Gou, W. et al. Tunable nonreciprocal quantum transport through a dissipative Aharonov-Bohm ring in ultracold atoms. *Phys. Rev. Lett.* **124**, 070402 (2020).
28. Ren, Z. et al. Chiral control of quantum states in non-Hermitian spin-orbit-coupled fermions. *Nat. Phys.* **18**, 385–389 (2022).
29. Han, P. R. et al. Exceptional entanglement phenomena: non-Hermiticity meeting non-classicality. *Phys. Rev. Lett.* **131**, 260201 (2023).
30. Dembowski, C. et al. Experimental observation of the topological structure of exceptional points. *Phys. Rev. Lett.* **86**, 787–790 (2001).
31. Zhou, H. et al. Observation of bulk Fermi arc and polarization half charge from paired exceptional points. *Science* **359**, 1009–1012 (2018).
32. Cerjan, A. et al. Experimental realization of a Weyl exceptional ring. *Nat. Photon.* **13**, 623–628 (2019).
33. Liu, J. J. et al. Experimental realization of Weyl exceptional rings in a synthetic three-dimensional non-Hermitian phononic crystal. *Phys. Rev. Lett.* **129**, 084301 (2022).

34. Zhen, B. et al. Spawning rings of exceptional points out of Dirac cones. *Nature* **525**, 354–358 (2015).
35. Wang, K. et al. Generating arbitrary topological windings of a non-Hermitian band. *Science* **371**, 1240–1245 (2021).
36. Wang, K., Dutt, A., Wojcik, C. C. & Fan, S. Topological complex-energy braiding of non-Hermitian bands. *Nature* **598**, 59–64 (2021).
37. Zhang, Q. et al. Observation of acoustic non-Hermitian Bloch braids and associated topological phase transitions. *Phys. Rev. Lett.* **130**, 017201 (2023).
38. Tang, W., Ding, K. & Ma, G. Direct measurement of topological properties of an exceptional parabola. *Phys. Rev. Lett.* **127**, 034301 (2021).
39. Su, R. et al. Direct measurement of a non-Hermitian topological invariant in a hybrid light-matter system. *Sci. Adv.* **7**, eabj8905 (2021).
40. Zhang, W. et al. Observation of non-Hermitian topology with non-unitary dynamics of solid-state spins. *Phys. Rev. Lett.* **127**, 090501 (2021).
41. Cao, M.-M. et al. Probing complex-energy topology via non-Hermitian absorption spectroscopy in a trapped ion simulator. *Phys. Rev. Lett.* **130**, 163001 (2023).
42. Wu, Y. et al. Observation of the knot topology of non-Hermitian systems in a single spin. *Phys. Rev. A* **108**, 052409 (2023).
43. Tang, W. et al. Exceptional nexus with a hybrid topological invariant. *Science* **370**, 1077–1080 (2020).
44. Tang, W., Ding, K. & Ma, G. Realization and topological properties of third-order exceptional lines embedded in exceptional surfaces. *Nat. Commun.* **14**, 6660 (2023).
45. Patil, Y. S. S. et al. Measuring the knot of non-Hermitian degeneracies and non-commuting braids. *Nature* **607**, 271–275 (2022).
46. Minganti, F., Miranowicz, A., Chhajlany, R. W. & Nori, F. Quantum exceptional points of non-Hermitian Hamiltonians and Liouvillians: the effects of quantum jumps. *Phys. Rev. A* **100**, 062131 (2019).
47. Teixeira, W. S., Vadimov, V., Mörstedt, T., Kund, S. & Möttönen, M. Exceptional-point-assisted entanglement, squeezing, and reset in a chain of three superconducting resonators. *Phys. Rev. Res.* **5**, 033119 (2023).
48. Wu, Y. et al. Third-order exceptional line in a nitrogen-vacancy spin system. *Nat. Nanotechnol.* **19**, 160–165 (2024).
49. Chen, W., Özdemir, Ş. K., Zhao, G., Wiersig, J. & Yang, L. Exceptional points enhance sensing in an optical microcavity. *Nature* **548**, 192–196 (2017).
50. Li, Z.-Z., Chen, W., Abbasi, M., Murch, K. W. & Whaley, K. B. Speeding up entanglement generation by proximity to higher-order exceptional points. *Phys. Rev. Lett.* **131**, 100202 (2023).

Acknowledgements

Author contributions

S.-B.Z. proposed the theoretical model and conceived the experiment. P.-R.H., W.N., X.-J.H. supervised by Z.-B.Y. and S.-B.Z., carried out the experiment. P.-R.H., R.-H.Z., S.-B.Y., F.W., Q.-P.S., C.-P.Y., and S.-B.Z. analyzed the data. S.-B.Z., Z.-B.Y., and C.-P.Y. co-wrote the paper. All authors contributed to the interpretation of observed phenomena and helped to write the paper.

Competing interests

The authors declare no competing interests.

Additional information

Supplementary information The online version contains supplementary material available at https://doi.org/10.1038/s41467-024-54662-8.

Correspondence and requests for materials should be addressed to Zhen-Biao Yang, Chui-Ping Yang or Shi-Biao Zheng.

Peer review information *Nature Communications* thanks the anonymous reviewer(s) for their contribution to the peer review of this work. A peer review file is available.

Reprints and permissions information is available at http://www.nature.com/reprints

Publisher's note Springer Nature remains neutral with regard to jurisdictional claims in published maps and institutional affiliations.